COMMUNICATIONS ON
PURE AND APPLIED ANALYSIS
Volume **1**, Number **4**, October **2002**

Website: http://AIMsciences.org

pp. **1–14**

A SEMI-IMPLICIT MOVING MESH METHOD FOR THE FOCUSING NONLINEAR SCHRÖDINGER EQUATION

Hector D. Ceniceros

Department of Mathematics
University of California
Santa Barbara California, 93106

(Communicated by ???)

Abstract. An efficient adaptive moving mesh method for investigation of the semi-classical limit of the focusing nonlinear Schrödinger equation is presented. The method employs a dynamic mesh to resolve the sea of solitons observed for small dispersion parameters. A second order semi-implicit discretization is used in conjunction with a dynamic mesh generator to achieve a cost-efficient, accurate, and stable adaptive scheme. This method is used to investigate with highly resolved numerics the solution's behavior for small dispersion parameters. Convincing evidence is presented of striking regular space-time patterns for both analytic and non-analytic initial data.

1. **Introduction.** Consider the initial value problem for focusing nonlinear Schrödinger equation (FNLS) in one space dimension:

$$i\epsilon\psi_t + \frac{1}{2}\epsilon^2\psi_{xx} + |\psi|^2\psi = 0 \qquad -\infty < x < \infty\ , \quad t > 0, \tag{1}$$

$$\psi(x,0) = A_0(x)e^{iS_0(x)/\epsilon}\ , \tag{2}$$

for small ϵ and where $A_0(x)$ is the initial amplitude and $S_0(x)$ is the real initial phase. The FNLS is connected to many applications in science and technology. For example, it has been tied to the motion of a vortex filament in inviscid impressible fluids with the celebrated transformation of Hasimoto [7] and is has also been used to model the fiber architecture of aortic heart valve leaflets [13].

The limit $\epsilon \to 0$ is called the semi-classical limit and considerable attention has been given recently to the investigation of its existence and structure [12, 2, 5, 9]. The dynamics of the limit is an open problem. While there is an apparent general belief that the weak limit does exist and that the solution develops a quite regular pattern for analytic initial conditions there is lack of consensus [2, 5] for such regularity in the case of non-analytic data. One of our goals here is to contribute to a clarification of the solution's behavior for the non-analytic case.

Numerically this is a notoriously difficult problem; extremely high resolution (both in space and time) is required to capture accurately the solution's strong self-focusing and a fairly localized "sea" of solitons whose wavelengths are $O(\epsilon)$. Since the computational domain has to be a large spatial interval to avoid boundary

1991 *Mathematics Subject Classification.* 35Q55, 65M50.

Key words and phrases. Semi-classical limit, dynamically adaptive mesh, modulational instability.

effects (we assume here that $A_0(x)$ decays rapidly to zero or that it has compact support) uniform meshes become inefficient for small ϵ. To make things worse, the $\epsilon = 0$ problem is ill-posed. This can be viewed by using two of the infinitely many conservation laws the FNLS has, namely (see e.g. [5])

$$\rho_t + \mu_x = 0 \ , \tag{3}$$

$$\mu_t + [\frac{\mu^2}{\rho} - \frac{\rho^2}{2}]_x = \frac{\epsilon^2}{4}[\rho(log\rho)_{xx}]_x \ , \tag{4}$$

where $\rho = |\psi|^2$ and $\mu = -i\frac{\epsilon}{2}(\bar{\psi}\psi_x - \psi\bar{\psi}_x)$ and the bar denotes complex conjugate. For $\epsilon = 0$, (3) and (4) become an elliptic system which is exactly Euler equations in one-dimensional gas dynamics with a strange pressure law: the pressure decreases as the density (ρ) increases. This underlying ill-posedness gives rise to the Benjamin-Feir or modulational instability and brings high sensitivity of the solution to round-off error noise for sufficiently small ϵ.

The small length scale, the localization of the solution, and the need of a relatively large computational domain call for an adaptive method. Cleverly designed moving mesh methods have been used to study the finite-time blow-up of the FNLS in higher dimensions [3, 14]. But, as we illustrate in this work, moving mesh methods are difficult to apply in the non-singular but highly dispersive one-dimensional FNLS. One of the main difficulties stems from the introduction of the mesh advection term into the underlying FNLS. This advection term, absent for a uniform mesh, can become dominant for small ϵ and lead to innacuracies and instabilities. Another main difficulty is that solution develops large derivatives in a highly oscillatory region and not in one isolated point. In fact, we find that because of the latter a standard static adaptive approach, i.e. remeshing at fixed time intervals, fails.

Here, we construct a stable and cost efficient moving mesh method for (1)-(2). Our building block is the mesh generator proposed by Ceniceros and Hou [4] combined with a semi-implicit second order time discretization and a fourth order approximation of the mesh advection term. The semi-implicit scheme is chosen with asymptotic high modal damping to stabilize the advection term. No artificial smoothing or interpolation is applied at all. Using this robust adaptive method we present convincing evidence that the behavior of the FNLS solutions as ϵ goes to zero appear to be surprisingly regular for both analytic and non-analytic initial data. This confirms independently and with superior resolution the results reported in [5]. Most importantly, the highly resolved numerics make transparent the space-time regularity of the solution for *non-analytic* initial conditions and shed some light on the limit structure.

The organization of this paper is as follows. In Section 2 the numerical method is described in detail and the issues of time and spatial discretizations are discussed as they affect stability and performance. The numerical results are presented in Section 3 and some concluding remarks are given in Section 4.

2. **The Numerical Method.**

There are three main components in our numerical method that determine its stability and overall efficacy (resolution vs computational cost): the dynamic mesh generator (or moving mesh PDE) and the time and spatial discretizations. We address separately these components in this section.

2.1. **The Moving Mesh.** We consider the FNLS in the spatial interval $[-M, M]$ where $M > 0$ is sufficiently large. A moving mesh is produced via a continuous time-dependent mesh map or coordinate transformation $x(\xi, t)$ from $[-M, M]$ to itself. Here ξ is called the computational or logical variable. The goal is to find a mesh map $x(\xi, t)$ to spread the very localized solitons of wavelength $O(\epsilon)$ along the whole computational domain $[-M, M]$. Viewed in the computational space the solution $\Psi(\xi, t) = \psi(x(\xi, t), t)$ would be much less localized and therefore could be resolved more efficiently.

Letting $\sigma = 1/x_\xi$, the evolution equation (1) is transformed to:

$$i\epsilon\dot{\Psi} + \frac{1}{2}\epsilon^2\sigma(\sigma\Psi_\xi)_\xi + |\Psi|^2\Psi = i\epsilon\dot{x}\sigma\Psi_\xi \tag{5}$$

where the dot stands for the time derivative keeping ξ fixed.

Recently, Ceniceros and Hou [4] proposed a variant of the traditional Winslow map and combined it with the PDE moving mesh idea of Huang and Russell [8] to produce an effective dynamic mesh for potentially singular problems. The mesh generator in [4] is given, for the one dimensional case, by the nonlinear PDE:

$$\dot{x} = (wx_\xi)_\xi, \tag{6}$$

where w is a solution-dependent monitor function which in our context would have the form:

$$w = \sqrt{1 + \beta^2|\Psi_\xi|^2 + f^2(|\Psi|)}, \tag{7}$$

where $\beta = \beta(t)$ is a time-dependent scaling and f is a function that can be chosen to reflect the leading order dynamics of the underlying problem, specially when there is finite-time singularity formation, or to penalize for large values of $|\Psi|$.

For the FNLS on $[-M, M]$ we would like to have a mesh map for which

$$\|\Psi_\xi\|_\infty = O\left(\frac{\|\Psi\|_\infty}{2M}\right), \tag{8}$$

so that the localized regions will be spread completely in $[-M, M]$. Taking $f \equiv 0$, and using $w \sim \text{const}/x_\xi$, and $\Psi_\xi = \psi_x x_\xi$ we find that (8) implies

$$\beta(t) = O\left((2M)^2\frac{\|\psi_x\|_\infty}{\|\psi\|_\infty^2}\right). \tag{9}$$

Because the FNLS in 1D does not exhibit finite-time singularity formation one can choose f to penalize for large values of $|\Psi|$ and improve the mesh distribution. The simplest choices would be $f = \alpha|\Psi|$ or $f = \alpha|\Psi|^2$, where α is a constant. The latter choice preserves the scaling invariance of the FLNS: $\psi(x, t) \to \frac{1}{\lambda}\psi(\frac{x}{\lambda}, \frac{t}{\lambda^2})$ just as in the moving mesh invariant method of Budd, Huang, and Russell [3] used for the radially symmetric problem with finite-time blow-up. In our present context, we observe no significant difference in the mesh quality for these two choices of f. We do observe however that a time-dependent β appears to give rise to strong mesh advection which is difficult to resolve and that ultimately affects severely the performance of the adaptive method. Hence, we choose a constant scaling β and the monitor function is given by

$$w = \sqrt{1 + \beta^2|\Psi_\xi|^2 + \alpha^2|\Psi|^4}, \tag{10}$$

$$\beta = (2M)^2\frac{\|\psi_{0x}\|_\infty}{\|\psi_0\|_\infty^2}c, \tag{11}$$

where both c and α are constants selected so that the initial data is well spread in the computational domain and $\psi_0 = \psi(x, 0)$.

2.2. **Time Discretization.** The coupled moving mesh-FNLS system is given by (recall $\sigma = 1/x_\xi$):

$$\dot{x} = (w x_\xi)_\xi, \tag{12}$$

$$\dot{\Psi} = i\frac{\epsilon}{2}\sigma(\sigma\Psi_\xi)_\xi + i\frac{1}{\epsilon}|\Psi|^2\Psi + \dot{x}\sigma\Psi_\xi. \tag{13}$$

This is a very stiff system due to the mesh equation and the second derivative (dispersive) term in the FNLS. One numerical approach [8] is to solve (12) and (13) alternately in time; first, (12) is solved for one time step to obtain a new mesh and then this new mesh is turn used to solve (13) also for one time step. This procedure is repeated every time step.

In [4], the following discretization was used to compute the moving mesh equation (12) at every time step:

$$\frac{x^{n+1} - x^n}{\Delta t} = a^n x_{\xi\xi}^{n+1} + (w^n x_\xi^n)_\xi - a^n x_{\xi\xi}^n, \tag{14}$$

where $a^n = \max w^n$ and Δt is the time step size. Discretizing the spatial derivatives with standard second order finite differences one gets a tridiagonal system which can be inverted fast at the optimal low cost of $O(N)$ operations, where N is the total number of grid points. The semi-implicit discretization (14) is only a first order accurate approximation to (12). But the accuracy with which the moving mesh PDE is solved does not affect the accuracy of the underlying solution Ψ. In fact one can regard (14), with the corresponding discretizations for the spatial derivatives, as our dynamic mesh generator and assume that the mesh is computed exactly. The moving mesh PDE (12) is a highly nonlinear diffusion equation. The high diffussivity of this equation and the numerical dissipation associated with a first order scheme make (14) a very stable and robust discretization.

Due to the dispersive nature of the FNLS plus the introduction of the mesh advection term $\dot{x}\sigma\Psi_\xi$ (not present when a static uniform mesh is used) it is difficult to obtain accurate and stable semi-implicit discretizations for (13) and fully implicit discretizations would too costly. To find a stable and cost efficient scheme we use as a guide the multi-step implicit/explicit (IMEX) methods studied by Ascher, Ruuth, and Wetton [1]. We consider two second order IMEX methods applied to (13). The semi backward difference formula (SBDF) scheme, also called extrapolated Gear:

$$\begin{aligned}\frac{1}{2\Delta t}[3\Psi^{n+1} - 4\Psi^n + \Psi^{n-1}] = i\frac{\epsilon}{2}\sigma^{n+1}(\sigma^{n+1}\Psi_\xi^{n+1})_\xi \\ + 2\left[i\frac{1}{\epsilon}|\Psi^n|^2\Psi^n + \dot{x}^n\sigma^n\Psi_\xi^n\right] \\ - \left[i\frac{1}{\epsilon}|\Psi^{n-1}|^2\Psi^{n-1} + \dot{x}^{n-1}\sigma^{n-1}\Psi_\xi^{n-1}\right],\end{aligned} \tag{15}$$

and the more popular Crank-Nicolson Leap Frog (CNLF) scheme:

$$\begin{aligned}\frac{1}{2\Delta t}[\Psi^{n+1} - \Psi^{n-1}] = i\frac{\epsilon}{4}\sigma^{n+1}(\sigma^{n+1}\Psi_\xi^{n+1})_\xi + i\frac{\epsilon}{4}\sigma^{n-1}(\sigma^{n-1}\Psi_\xi^{n-1})_\xi \\ + i\frac{1}{\epsilon}|\Psi^n|^2\Psi^n + \dot{x}^n\sigma^n\Psi_\xi^n.\end{aligned} \tag{16}$$

It was found in [1] that SBDF has the mildest stability constraint among second order IMEX schemes for the prototype *advection-diffusion* equation $u_t = au_x + \nu u_{xx}$ and that it also has strong asymptotic high frequency decay which eliminates aliasing errors when pseudo-spectral derivatives are used. In contrast, CNLF has a smaller truncation error than SBDF but its asymptotic high frequency decay tends to 1.

A stability analysis for either (15) or (16) is extremely difficult however one can gain some insight by doing von Neumann analysis (see for example [15]) for the schemes applied to the linear *advection-dispersion* equation

$$\psi_t = i\epsilon\psi_{xx} + \psi_x, \tag{17}$$

where ϵ is a constant that measures the dispersion/advection ratio. The von Neumann amplification factor g for SBDF applied to (17) using standard second order discretization for the spatial derivatives satisfies the quadratic equation

$$(3 + i\frac{8\lambda\epsilon}{h}\sin^2\frac{\theta}{2})g^2 - 2(2 + i2\lambda\sin\theta)g + 1 + i2\lambda\sin\theta = 0 \qquad \theta \in [0, \pi], \tag{18}$$

where $\lambda = \Delta t/h$ and h is the mesh size. On the other hand for CNLF we have:

$$(1 + i\frac{4\lambda\epsilon}{h}\sin^2\frac{\theta}{2})g^2 - i2\lambda\sin\theta g - (1 - i\frac{4\lambda\epsilon}{h}\sin^2\frac{\theta}{2}) = 0 \qquad \theta \in [0, \pi]. \tag{19}$$

A plot of $|g|$ against θ for the largest root of the amplification factor for both schemes is presented in Figure 1. Here, $\epsilon = 0.05$, $h = 0.01$, and $\lambda = 0.5$. The SBDF has a strong high frequency decay whereas CNLF has none. Thus, it is reasonable to expect that SBDF would produce a more stable scheme for the FNLS coupled with the moving mesh. Indeed, through numerical experiments we find that SBDF is quite stable but CNLF experiences instabilities. It is conceivable that these instabilities are due to the high frequency components (which CNLF fails to damp) of the truncation error introduced by the discretization of the mesh advection term (we elaborate more on this in the next section). Finally, we note that the von Neumann analysis reveals that for $\epsilon = 0$ SBDF is unstable whereas CNLF is stable but only marginally ($|g| = 1$) under the condition $\lambda \leq 1$. Thus, we anticipate that as ϵ gets smaller SBDF would require a smaller λ for stability.

2.3. **Spatial Discretization.** Any particular choice of spatial discretization for the FNLS (13) affects the stability, accuracy, and cost of the overall adaptive method. Pseudo-spectral approximations have been common in FNLS computations [2, 5]. With a uniform mesh, semi-implicit discretizations such as SBDF or CNLF can be inverted at a cost of $O(\log_2 N)$ operations using the Fast Fourier Transform (FFT) (see e.g [5]). However, FFT cannot be used for the variable coefficient system produced by a non-uniform mesh. In this case one would have to employ an iterative method at each time-step which would increase the computational cost and may introduce some numerical instability.

It is natural to ask whether a discretization of the type (14), i.e. extracting a constant coefficient leading order term and discretizing it implicitly, can be used for (13). This would transform the implicit part into a constant coefficient term that can be inverted as easily as for a uniform mesh. Unfortunately, we have found through numerical experiments that such a discretization for (13) is highly unstable, in contrast to the very stable behavior of the scheme in the case of the moving mesh equation (14). This behavior disparity can be accounted for by the

high frequency mismatch between the variable coefficient term and the constant coefficient one, the difference being treated explicitly. On one hand the moving mesh equation is strongly dissipative with additional numerical dissipation introduced by the first order Euler discretization. This high dissipation keeps under control the high frequency components of the explicitly-treated difference. On the other hand, the FNLS (13) is dispersive and there is no natural damping to the high frequency components of the difference. We find that a CNLF discretization of the type (14) for the FNLS is unstable whereas the high frequency damping of SBDF produces a stable discretization *only* if the solution is sufficiently smooth. Hence, a discretization of the type (14) for non-dissipative equations should be avoided.

A second order discretization in space of the implicit term $\sigma^{n+1}(\sigma^{n+1}\Psi_\xi^{n+1})_\xi$ appears to be more cost effective and robust than a spectral discretization when a non-uniform mesh is used, particularly when the solution has large derivatives and/or is not analytic. But special care must be taken to discretize the mesh advection term $\dot{x}\psi_x$. As pointed out by Li, Petzold, and Ren [10] this term, absent for a uniform mesh, can introduce instabilities and degrade the accuracy to the extent that the moving mesh results are inferior to a corresponding uniform mesh computation. For example, if a centered approximation is used to discretize ψ_x one has [10]

$$\begin{aligned}\frac{\psi_{j+1}-\psi_{j-1}}{x_{j+1}-x_{j-1}} &= \psi_x + \frac{1}{2}h^2(x_{\xi\xi}\psi_{xx} + \frac{1}{3}x_\xi^2\psi_{xxx}) + \dots \\ &= \psi_x + \frac{1}{2}(\Delta x_j)^2(\frac{x_{\xi\xi}}{x_\xi^2}\psi_{xx} + \frac{1}{3}\psi_{xxx}) + \dots ,\end{aligned} \tag{20}$$

where $\Delta x_j = x_{j+1} - x_j$ and h is the mesh size in ξ. Thus, the truncation error introduces a numerical diffusion with a variable coefficient $x_{\xi\xi}/x_\xi^2$ that could be negative and hence destabilizing. Moreover, as remarked also in [10], large mesh variations (large compressions) would imply a significant truncation error ($x_{\xi\xi}/x_\xi^2$ could be very large!). Indeed, we implemented the moving mesh method discretizing the advection term ψ_x with a centered second order finite difference and observed that both the accuracy and the stability deteriorate quickly.

At this point one could think that a static adaptive mesh approach in which a new mesh map is computed at fixed time intervals is preferable for this problem. Using the mesh generator (12) solved to steady state we have found that such a static approach fails as soon as sea of solitons appears.

Li, Petzold, and Ren [10] propose two strategies for overcoming the difficulties tied to the moving mesh advection term . One is to use high order upwinding schemes [11] and the other is to distribute more nodes to the unstable region. Here we opt for an alternative: discretize ψ_x with a standard fourth order finite difference to reduce the truncation error and rely on the SBDF asymptotic damping to stabilize this term.

With these observations, our fully discrete adaptive method can be written as follows. First we have the moving mesh generator:

$$\begin{aligned}\frac{x^{n+1}-x^n}{\Delta t} &= a^n\frac{x_{j+1}^{n+1}-2x_j^{n+1}+x_{j-1}^{n+1}}{h^2} - a^n\frac{x_{j+1}^n-2x_j^n+x_{j-1}^n}{h^2} \\ &\quad + \frac{1}{h^2}\left[w_{j+1/2}^n(x_{j+1}^n-x_j^n) - w_{j-1/2}^n(x_j^n-x_{j-1}^n)\right],\end{aligned} \tag{21}$$

where $a^n = w^n$, and the monitor function w is given by (10). As it is common practice in adaptive methods w is smoothed with a low pass filter $w_j \leftarrow (w_{j-1} + 2w_j + w_{j+1})/4$ applied four times. Initially, this equation is solved to steady state and after this only for one step at a time. Once x^{n+1} is obtained from (21) we compute $\sigma^{n+1} = 1/x_\xi^{n+1}$ and the mesh speed $\dot{x}_j = (x_j^{n+1} - x_j^{n-1})/(2\Delta t)$ and use them to update Ψ with the SBDF scheme:

$$\begin{aligned}\frac{1}{2\Delta t}[3\Psi_j^{n+1} - 4\Psi_j^n + \Psi_j^{n-1}] = \\ i\frac{\epsilon\sigma_j^{n+1}}{2h^2}\left[\sigma_{j+1/2}^{n+1}(\Psi_{j+1}^{n+1} - \Psi_j^{n+1}) - \sigma_{j-1/2}^{n+1}(\Psi_j^{n+1} - \Psi_{j-1}^{n+1})\right] \\ +2\left[\frac{i}{\epsilon}|\Psi_j^n|^2\Psi_j^n + \dot{x}_j^n\frac{\Psi_{j-2}^n - 8\Psi_{j-1}^n + 8\Psi_{j+1}^n - \Psi_{j+2}^n}{x_{j-2}^n - 8x_{j-1}^n + 8x_{j+1}^n - x_{j+2}^n}\right] \\ -\left[\frac{i}{\epsilon}|\Psi_j^{n-1}|^2\Psi_j^{n-1} + \dot{x}_j^{n-1}\frac{\Psi_{j-2}^{n-1} - 8\Psi_{j-1}^{n-1} + 8\Psi_{j+1}^{n-1} - \Psi_{j+2}^{n-1}}{x_{j-2}^{n-1} - 8x_{j-1}^{n-1} + 8x_{j+1}^{n-1} - x_{j+2}^{n-1}}\right],\end{aligned} \tag{22}$$

with the boundary condition $\Psi = 0$. Note that the mesh advection term is discretized using fourth order finite differences.

Because Ψ is a complex-valued function one cannot use a tridiagonal solver to find Ψ^{n+1}. Instead we write $\Psi = U + iV$, where U and V are real-valued functions and get for (22) an equivalent coupled linear system of the form:

$$3U_j^{n+1} + \frac{\Delta t\epsilon}{h^2}(\alpha_j V_{j-1}^{n+1} - \beta_j V_j^{n+1} + \gamma_j V_{j+1}^{n+1}) = P_j, \tag{23}$$

$$3V_j^{n+1} - \frac{\Delta t\epsilon}{h^2}(\alpha_j U_{j-1}^{n+1} - \beta_j U_j^{n+1} + \gamma_j U_{j+1}^{n+1}) = Q_j, \tag{24}$$

where the coefficients α_j, β_j, and γ_j are known from the $(n+1)$st update of the moving mesh solution and P_j and Q_j are known from previous time step information. Solving (24) for V^{n+1} and substituting in (23) yields a pentadiagonal linear system for U^{n+1}. This system can be solved fast with a pentadiagonal solver [6] in $O(N)$ operations per time step. Once U^{n+1} has been found then V^{n+1} is computed from (24). The overall semi-implicit method maintains the same order of operations of an explicit method.

3. Numerical Results.

We consider two types of initial conditions, one is analytic with zero phase and the other one is non-analytic with non-zero phase. Our spatial and physical domain is $[-10, 10]$ ($M = 10$).

3.1. Analytic initial condition.

We consider first the zero-phase analytic initial condition [5]:

$$A_0(x) = e^{-x^2}, \quad S_0(x) = 0\ , \tag{25}$$

and take $\epsilon = 0.05$. Figure 2 shows in close-up a sequence of snap-shots of $\rho = |\psi|^2$ at different times. The plotted results are obtained using the moving mesh adaptive method with two different resolutions: $N = 512$, $\Delta t = 1 \times 10^{-4}$ and $N = 1024$, $\Delta t = 5 \times 10^{-5}$. The results are indistinguishable within plotting resolution and illustrate the convergence of the method. The solution first self-focuses around $t = 0.45$, see Figure 2(a), forming a sharp and very localized spike. After this

self-focusing solitons of wavelength $O(\epsilon)$ are produced forming a clearly separated oscillatory region.

Figure 3 shows the real part of ψ in both the physical (displaying the position of the mesh points) and the computational domain. The moving mesh achieves a maximum compression ($\min x_\xi$) of 1.57×10^{-2}. Note that the adaptive mesh map completely spreads the solution in the whole computational interval yielding a much less localized function that can be effectively resolved with relatively few nodes. A uniform mesh would require 32768 nodes to achieve the same resolution. Two numerical approximations of $\rho = |\psi|^2$ at $t = 0.9$, one using the adaptive mesh and $N = 1024$, $\Delta t = 5 \times 10^{-5}$ and the other the pseudo-spectral method in [5] with a uniform mesh and $N = 32768$, $\Delta t = 1 \times 10^{-5}$, are compared in Figure 4. The approximations coincide within plotting resolution.

We now reduce ϵ to 0.025. Figure 5 presents $\rho = |\psi|^2$ plotted at the same times as those chosen for $\epsilon = 0.5$ (Figure 2). The smaller ϵ demands a much higher resolution both in space and time because, as predicted by WKB theory, the length scale shrinks. We take $N = 4096$ and $\Delta t = 2.5 \times 10^{-6}$. Although high, the computational cost of the adaptive method is still a fraction of that required by a uniform mesh for such a small ϵ. A comparison with Figure 2 shows an astonishing regularity of the solution hinting the existence of a weak limit and in agreement with the numerical evidence presented in [5] where a very different numerical method was used. The solution behavior also resembles that of the pure soliton data studied by Miller and Kamvissis [12] who considered exact solutions for $\epsilon = 0.4$, 0.2, and, 0.1. Figures 2 and 5 show further that a clear limiting envelop emerges as ϵ is decreased.

The efficacy of the adaptive mesh is demonstrated in Figure 6 where the real part of ψ at $t = 1.0$ is plotted in both the physical and the computational domain. Note how the adaptive mesh effectively stretches out the very localized and highly oscillatory region to give as a result a well-resolved solution in the computational space.

A ξ-t surface plot of the solution for $\epsilon = 0.025$ is given in Figure 7. The quiescent and the oscillatory regions and the strikingly regular pattern can be clearly distinguished. Note that this is a zoomed-in plot (because the computational ξ variable is used) of the very localized solution in the physical space where ρ is confined essentially to the interval $[-1, 1]$. A similar regularity was observed by Bronski and Kutz [2] who numerically studied the FNLS for $\epsilon = 0.1$.

3.2. **Non-analytic initial condition.** We now consider the following non-analytic initial condition [5]:

$$A_0(x) = \begin{cases} 1 - |x| & \text{if } |x| < 1 \\ 0 & \text{otherwise} \end{cases}, \quad S_0(x) = \frac{1}{\cosh(2x)}, \tag{26}$$

and start with $\epsilon = 0.05$. Resolving the solution for non-analytic conditions is a challenging task. The Fourier spectra shown in Figure 8 illustrate the slow algebraic modal decay of the initial condition and contrast the adaptive mesh transformation with the uniform mesh. The mesh map transforms the initial condition into one that has a fast smooth decay in the low band of the spectrum and lowers the amplitude of the algebraically decaying tail. For the uniform mesh the spectrum (of the physical initial condition) is very rough before setting to the asymptotic decay whose amplitude is larger than that for the adaptive mesh. This, tied to the

second differentiation in the FNLS, make uniform mesh computations require an extremely small Δt and a fairly large N.

We now present detailed adaptive mesh computations to investigate and clarify the solution's behavior for the non-analytic condition (26). A $\xi - t$ surface plot of ρ is given in Figure 9. The adaptive moving mesh zooms in the solution which in the physical domain is fairly localized to the interval $[-1, 1]$. Just like in the case of analytic initial conditions, the solution develops a quite regular pattern in space-time. This is in disagreement with the apparently irregular patterns reported by Bronski and Kutz [2].

One may think that perhaps the observed regularity is a numerical artifact produced by high frequency damping of the SBDF time stepping scheme (there is no other regularizing mechanism in our scheme). If this were the case, the numerical solution would change noticeably when changing the time and space resolutions and, more importantly, one would not observe convergence of the solution's spectrum.

To investigate this issue, we compare six resolutions with N equal to 512, 1024, 2048, 4096, 8192, and 16384 and Δt raging from 2×10^{-5} to 1.25×10^{-6}. As the resolutions are refined, we see a clear convergence to the regular pattern shown in Figure 9. To illustrate also the convergence and behavior of the numerical approximation in Fourier space we present in Figure 10 two different cases of refinement. Figure 10(a) shows the spectra of the real part of numerical approximation at $t = 0.5$ obtained using $N = 2048$ and two different time step sizes, $\Delta t = 2 \times 10^{-5}$ and $\Delta t = 1 \times 10^{-5}$. Figure 10(b) shows the spectra for two spatial approximations $N = 2048$ and $N = 4096$ and the same time step $\Delta t = 1 \times 10^{-5}$. In both cases the spectra corresponding to the different resolutions lie on top of one another and we can clearly observe the asymptotic algebraic modal decay of the solution. Thus, with these observations, it does appear that the regularity for the non-analytic data is genuine.

We consider now $\epsilon = 0.025$ to learn more about the structure of the possible (weak) limit. The initial condition is now more oscillatory because of the nonzero initial phase. A plot of the real part of the initial condition in the physical and computational spaces is given in Figure 11. A $\xi - t$ surface plot of ρ is provided in Figure 12. Again, the solution was checked using two different resolutions. The regularity is striking. One can also observe that the solitons begin to disperse around $t = 0.5$. Note that, as remarked in [5], the oscillatory region in space-time appears to approach the origin as ϵ is decreased. To conclude, we show in Figure 13 the real part of ψ in the physical and computational spaces at $t = 0.5$. The mesh map smoothly spreads out in the entire computational domain $[-10, 10]$ the highly oscillatory and localized solution. The adaptive mesh reaches a maximum compression of 2×10^{-2} in this case and the solution is perfectly well resolved in the computational domain. A comparable resolution with a uniform mesh would require 204800 nodes.

4. **Concluding Remarks.** The semi-classical limit of the focusing nonlinear Schrödinger equation presents a great computational challenge. Not only does the method have to resolve accurately the solution self-focusing (where a sharp "spike" is produced) but also the subsequent highly oscillatory regions of solitons with wavelengths of $O(\epsilon)$. One of the main difficulties in applying adaptive moving mesh methods to this problem originates from the introduction of the mesh advection term into the underlying equation which otherwise has no physical advection

at all. For small ϵ, the mesh advection can dominate the dispersion and, as a result, can lead to innacuracies and numerical instabilities. We have shown here that with the right semi-implicit scheme and a high order discretization for the mesh advection term it is possible to obtain accurate, cost-efficient, and stable moving mesh methods.

The numerical results reported here support with superior resolution the evidence given in [5] about the regularity and possible existence of the weak limit. Particularly important is the clarification of the solution's regular space-time patterns for *non-analytic* data for which there has not been a consensus [2, 5] and there is much ongoing investigation. We believe that the method presented here is a very valuable tool and can be used to learn more about the structure of the solutions limiting behavior for non-analytic initial conditions.

Acknowledgments. The author would like to thank Fei-Ran Tian and Luis Vega for insightful discussions regarding the nonlinear Schrödinger equation and Tom Hou for helpful suggestions and comments.

REFERENCES

[1] U. M. Ascher, S. J. Ruuth, and B. Wetton. Implicit-Explicit Methods for Partial Differential Equations, SIAM J. Numer. Anal., 32 (1995), 797–823.
[2] J. C. Bronski and J. N. Kutz. Numerical simulation of the semi-classical limit of the focusing nonlinear Schrödinger equation, Phys. Lett. A, 254 (1999), 325–336.
[3] C. J. Budd, W. Huang, and R. D. Russell. Moving mesh methods for problems with blow-up, SIAM J. Sci. Comput., 17 (1996), 305–327.
[4] H. D. Ceniceros and T. Y. Hou. An efficient dynamically adaptive mesh for potentially singular solutions, to appear in J. Comput. Phys., 2001.
[5] H. D. Ceniceros and F.-R. Tian. A numerical study of the semi-classical limit of the focusing nonlinear Schrödinger equation, to appear in Phys. Let. A, 2001.
[6] W. Cheney and D. Kincaid. " Numerical mathematics and computing," Brooks/Cole, 1985.
[7] H. Hasimoto. A soliton on a vortex filament, J. Fluid. Mech., 51 (1972), 477–485.
[8] W. Huang and R. D. Russell. Moving mesh strategy based on a gradient flow equation for two-dimensional problems, SIAM J. Sci. Comput., 20 (1999), 998–1015.
[9] S. Kamvissis, K. T.-R. McLaughlin, and P. Miller. Semiclassical soliton ensambles for the focusing nonlinear Schrödinger equation, preprint, 2000.
[10] S. Li, L. Petzold, and Y. Ren. Stability of moving mesh systems of partial differential equations, SIAM J. Sci. Comput., 20 (1998), 719–738.
[11] S. T. Li and L. R. Petzold. Moving mesh methods with upwinding schemes for time dependent PDEs, J. Comput. Phys., 131 (1997) 368–377.
[12] P. Miller and S. Kamvissis. On the semi-classical limit of the focusing nonlinear Schrödinger equation, Phys. Lett. A, 247 (1998), 75–86.
[13] C. Peskin and D. McQueen. Mechanical equilibrium determines the fractal fiber architecture of aortic heart valve leaflets, Am. J. Physiol., 266 (1994), H319–H328.
[14] W. Ren and X-P. Wang. An iterative grid redistribution method for singular problems in multiple dimensions, J. Comput. Phys., 159 (2000), 246–273.
[15] J. C. Strikwerda. " Finite Difference Schemes and Partial Differential Equations," Wadsworth & Brooks/Cole, 1989.

E-mail address: hdc@math.ucsb.edu

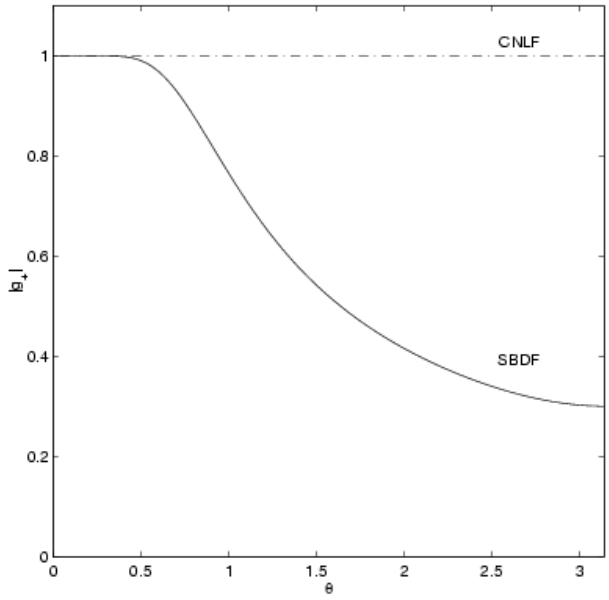

FIGURE 1. Comparison of the amplification factor for the SBDF (solid line) and the CNLF(dotted line) corresponding to the model equation $\psi_t = i\epsilon\psi_{xx} + \psi_x$. The parameters are $\epsilon = 0.5$, $h = 0.01$ and $\lambda = 0.5$.

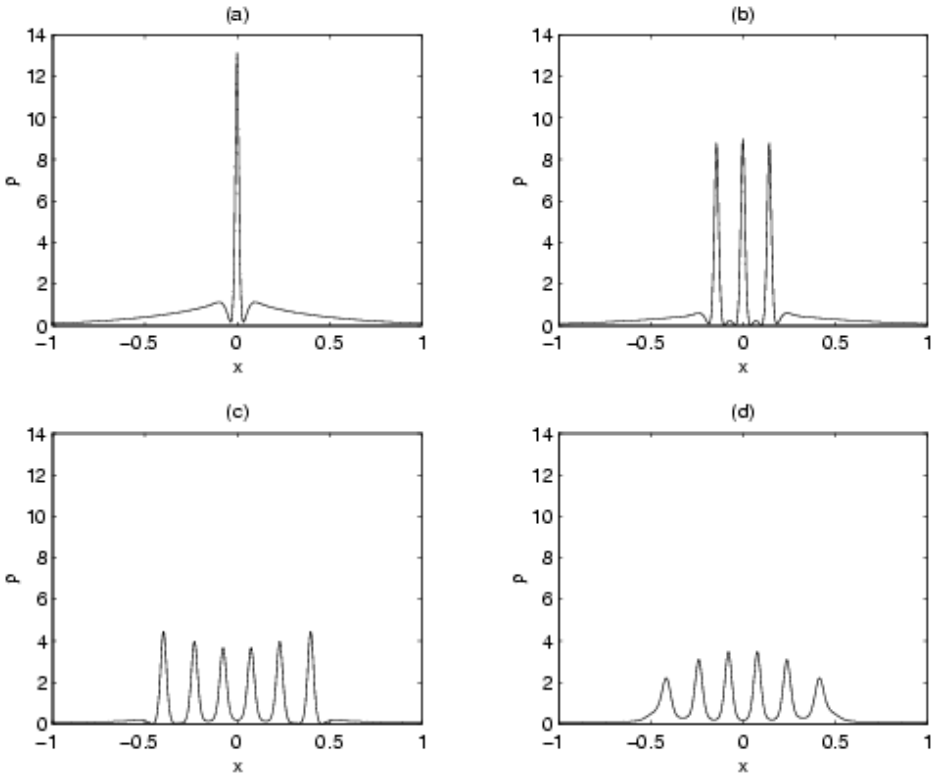

FIGURE 2. Close-up of $\rho = |\psi|^2$ in $[-1, 1]$ at different times for the Gaussian initial condition and $\epsilon = 0.05$. Two adaptive mesh resolutions are used: $N = 512$, $\Delta t = 1 \times 10^{-4}$ and $N = 1024$, $\Delta t = 5 \times 10^{-5}$. (a) $t = 0.45$, (b) $t = 0.60$, (c) $t = 0.90$, and (d) $t = 1.0$.

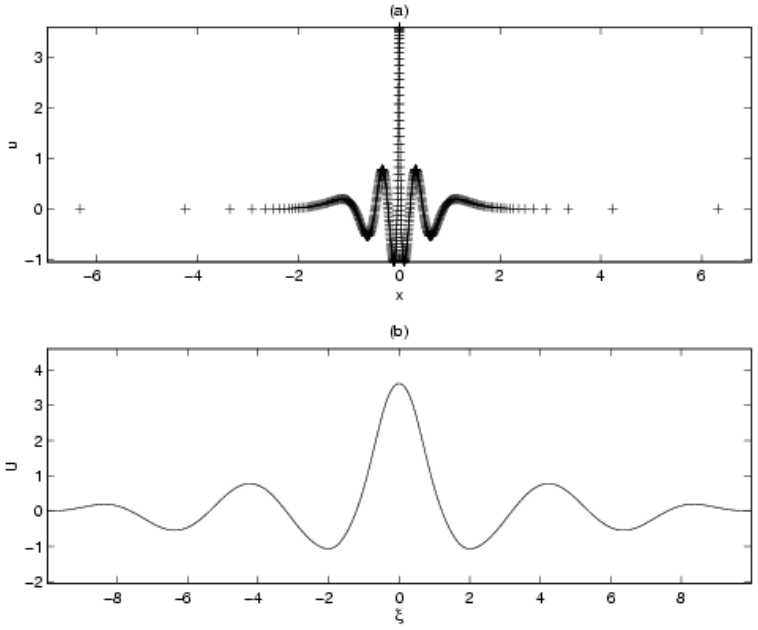

FIGURE 3. The real part of ψ at $t = 0.9$ for $\epsilon = 0.05$ in (a) the physical (showing the position of the adaptive mesh points) space and (b) the computational domain.

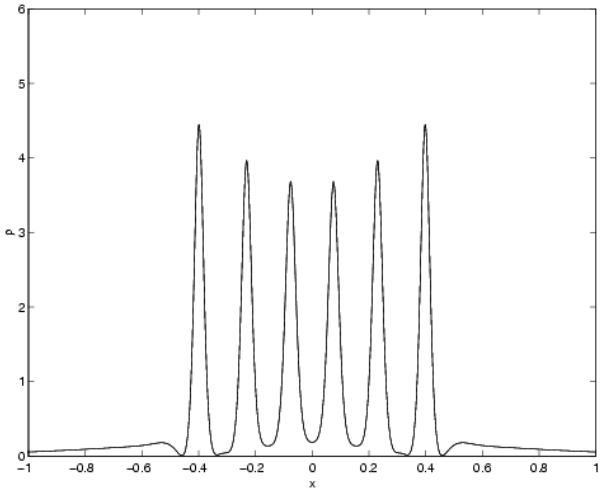

FIGURE 4. Close-up of $\rho = |\psi|^2$ in $[-1, 1]$ at $t = 0.9$, two numerical approximations are plotted together: one using the adaptive mesh and $N = 1024$, $\Delta t = 5 \times 10^{-5}$ and the other a uniform mesh and $N = 32768$, $\Delta t = 1 \times 10^{-5}$.

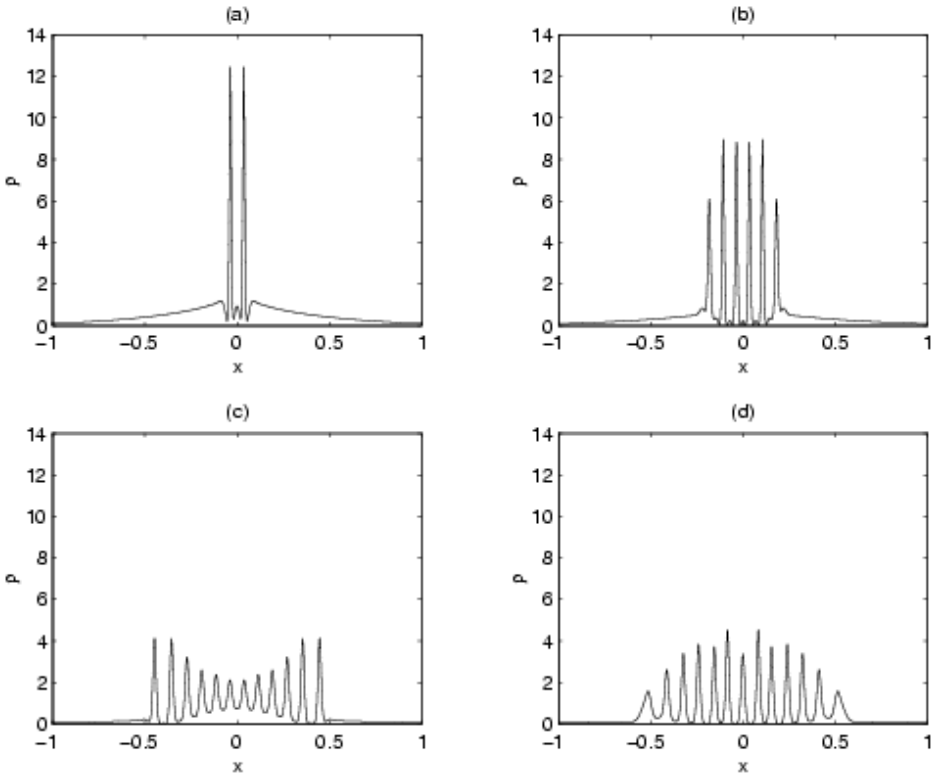

FIGURE 5. Close-up of $\rho = |\psi|^2$ in $[-1, 1]$ at different times for the Gaussian initial condition and $\epsilon = 0.025$. Adaptive mesh computation with $N = 1024$, $\Delta t = 5 \times 10^{-5}$. (a) $t = 0.45$, (b) $t = 0.60$, (c) $t = 0.90$, and (d) $t = 1.0$.

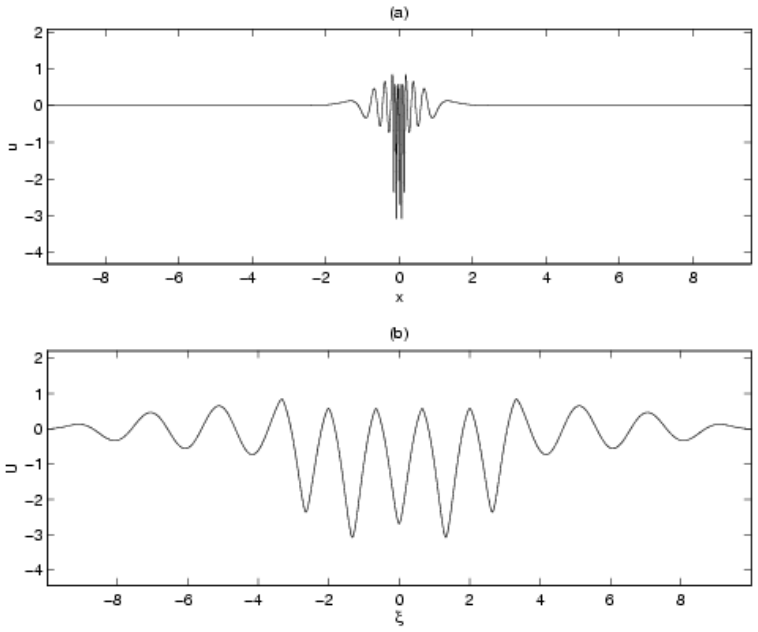

FIGURE 6. The real part of ψ at $t = 0.56$ for $\epsilon = 0.025$ in (a) the physical space and (b) the computational domain plotted with equal aspect ratio.

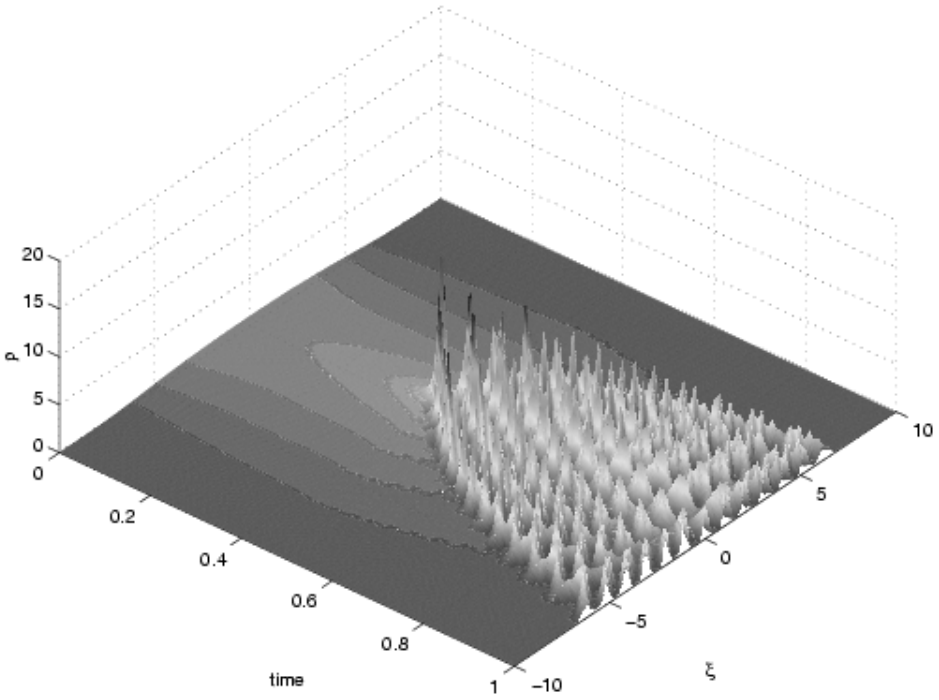

FIGURE 7. A ξ-t surface plot of $\rho = |\psi|^2$ for $\epsilon = 0.025$.

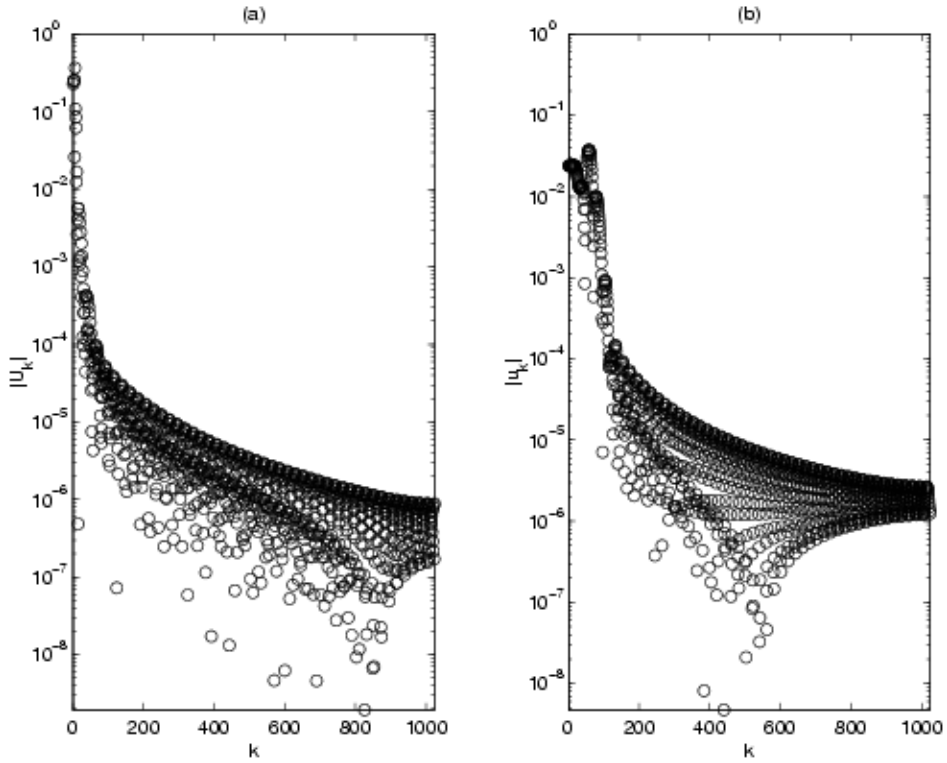

FIGURE 8. Fourier spectrum of the real part of the non-analytic initial condition for $\epsilon = 0.05$ obtained with $N = 2047$ and (a) the adaptive mesh, .i.e., the spectrum of $U(\xi) = u(x(\xi))$ is shown and (b) the uniform mesh.

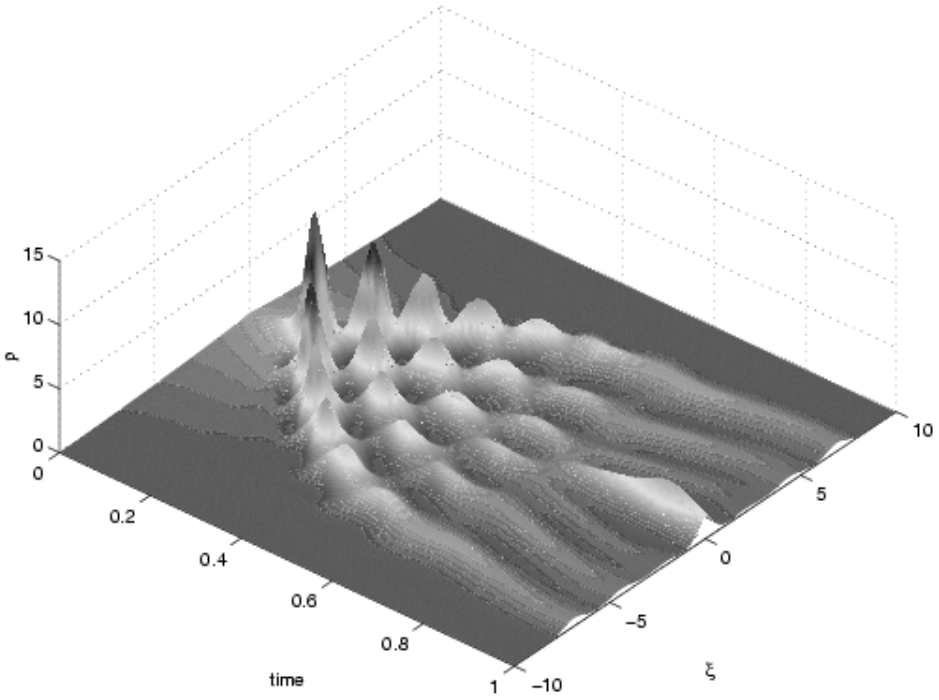

FIGURE 9. A $\xi - t$ surface plot of ρ for the non-analytic initial condition with $\epsilon = 0.05$.

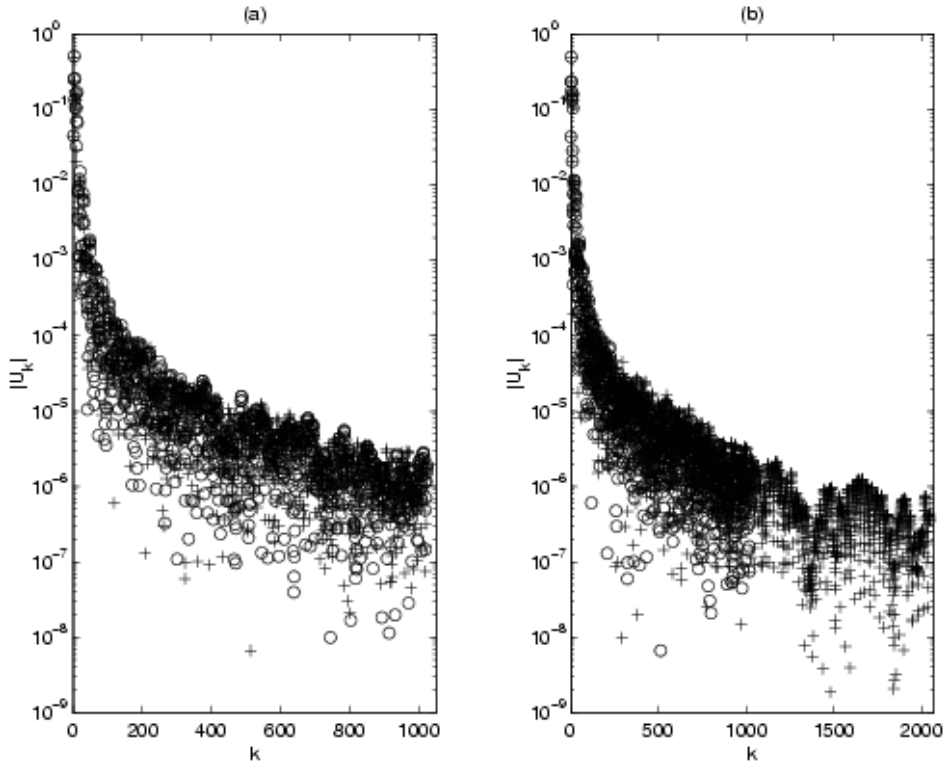

FIGURE 10. Fourier spectrum of $U(\xi)$ at $t = 0.5$ for two different resolutions. (a)$\Delta t = 2 \times 10^{-5}$(o) and $\Delta t = 1 \times 10^{-5}$ (+) for the same $N = 2048$. (b)$N = 2048$ (o) and $N = 4096$(+) for the same $\Delta t = 1 \times 10^{-5}$.

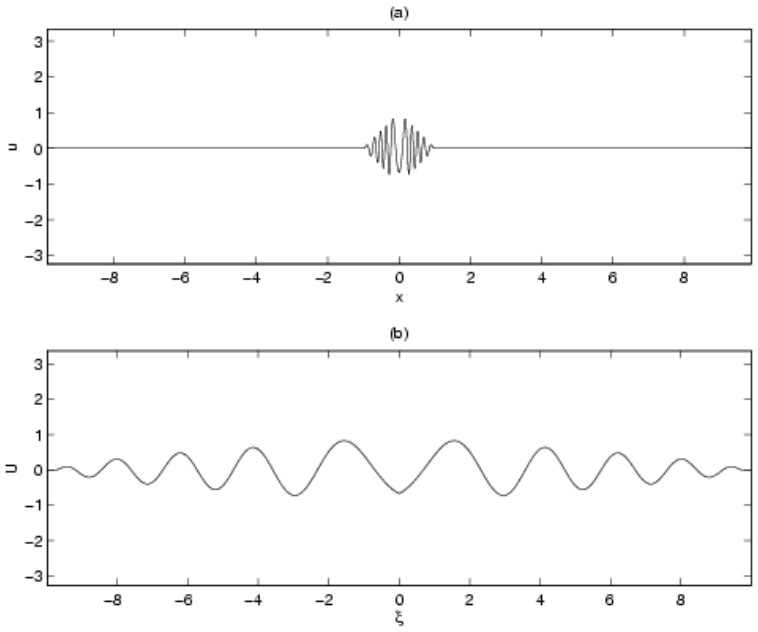

FIGURE 11. The real part of the non-analytic initial condition for $\epsilon = 0.025$ in (a) the physical space and (b) the computational domain with equal aspect ratio.

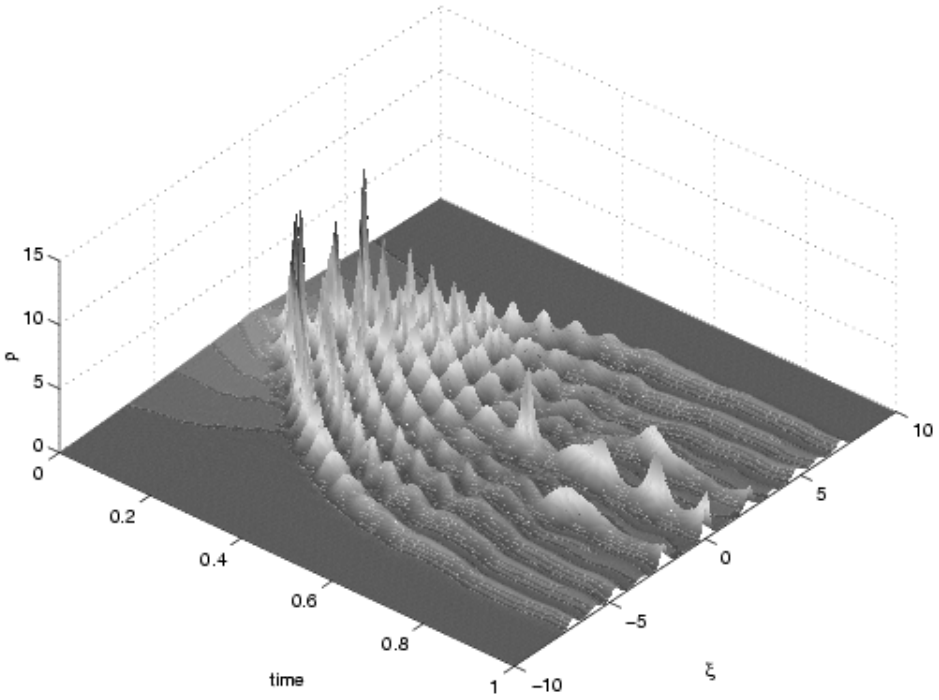

FIGURE 12. A $\xi - t$ surface plot of ρ for the non-analytic initial condition with $\epsilon = 0.025$.

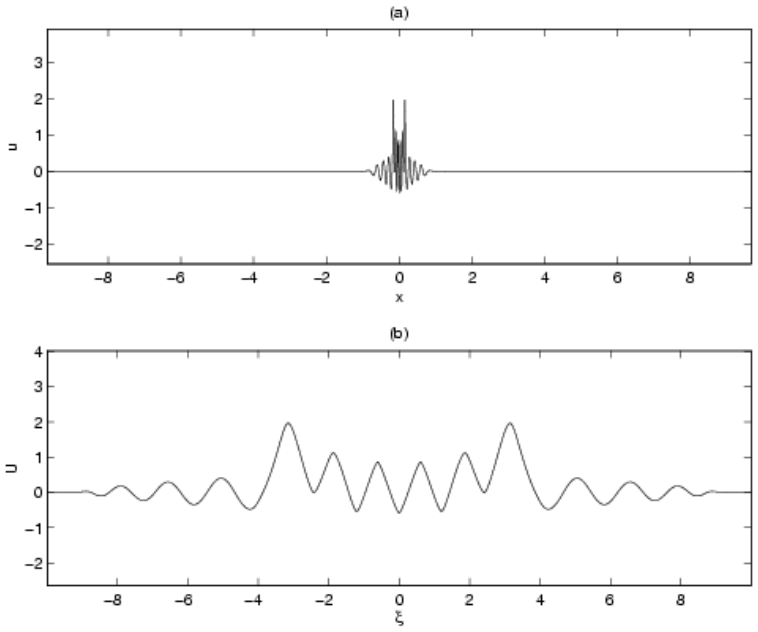

FIGURE 13. The real part of ψ for the non-analytic initial condition and $\epsilon = 0.025$ at $t = 0.0$ in (a) the physical space and (b) the computational domain with equal aspect ratio.